Pure Appl. Chem., Vol. 72, Nos. 1–2, pp. 269–279, 2000.

Interfacial chemistry in self-assembled nanoscale materials with structural ordering*

Jun Liu†, Glen E. Fryxell, Maoxu Qian, Li-Qiong Wang, and Yong Wang

Pacific Northwest National Laboratory, Richland, Washington 99352 USA

Abstract: This paper discusses the interfacial chemistry encountered in the self-assembly of ordered nanoscale materials based on surfactant liquid crystalline structures. The paper contains three sections. The first section gives a brief introduction to the interfacial chemistry in the co-assembly of surfactants and inorganic materials. The second section discusses the formation of inorganic–inorganic nanocomposites, the properties of such materials, and the interfacial atomic structures. The last section discusses hybrid nanoscale materials with functional monolayers, their interfacial chemistry, and their potential applications.

INTRODUCTION: ORDERED NANOSCALE MATERIALS BASED ON SURFACTANT LIQUID CRYSTALS

The successful synthesis of ordered nanoporous materials using surfactant liquid crystals as structural-directing agents [1,2] has opened new opportunities in designing novel nanoscale materials. These materials are characterized by nanoscale ordering, tunable domain size, and accessibility to a range of sophisticated structures. Since 1992 the development of ordered nanoporous materials has become a very active research area, and there have been many excellent publications related to the fundamental mechanism, the synthesis, and the properties of such materials [3–5].

Experimentally, the ordered nanoporous materials were prepared by mixing various surfactants with a wide range of ceramic precursors, and letting the mixtures react under mild hydrothermal conditions. Schematically, the surfactant molecules aggregate into micelles. The micelles further aggregate into ordered liquid crystalline structures. The inorganic precursors bind to the micellar head groups and further condense into a three-dimensional ceramic phase. Afterwards, the surfactant molecules may be removed by thermal or chemical means. This process will give a unique ordered nanoporous material.

The formation of the ordered nanostructure is determined by the fundamental interactions between the molecules with surfactant-like properties. These molecules include surfactant, lipids, copolymers, and proteins [6–8]. These amphiphilic molecules have two components: a hydrophobic tail group (or segment), and a hydrophilic head group (or segment). The major driving forces for forming well-defined aggregates are the hydrophobic attractions at the hydrocarbon–water interfaces and the hydrophilic ionic or steric repulsion between the head groups. A variety of ordered structures can be formed depending on the solution conditions (pH, temperature, or electrolyte concentrations). The equilibrium structures are determined by the thermodynamics of the self-assembly process and the inter- and intra-aggregate forces. Depending on the experimental conditions, spherical micelles, rod-like micelles, hexagonally ordered crystals, cubic crystals, lamellar phases, inverse micelles, or inverse micellar liquid crystals can be formed. Using the ordered liquid crystalline structures as the directing templates, a wide range of ordered nanocomposites can be synthesized [9]. More recently, the templates were extended to

Pure Appl. Chem.* **72, 1–331 (2000). An issue of reviews and research papers based on lectures presented at the 1st IUPAC Workshop on Advanced Materials (WAM1), Hong Kong, July 1999, on the theme of nanostructured systems.
†Corresponding author

include block copolymers [10]. The use of block copolymer surfactants further expanded pore size, and the possible compositional range. In addition to ordered nanoporous materials, it is possible to prepare other highly ordered nanocomposites based on these ordered liquid crystalline structures. These ordered composites will contain unique network structures and arrays of inter-penetrating phases to meet the structural requirements of "smart composites" with proper connectivity patterns, which are desirable in many applications, such as in piezoelectric transducers and pyroelectric detectors [11]. If a polymeric material is used as the template, the organic phase can be left behind to give a highly ordered nanocomposite [12]. Such ordered nanocomposites are difficult to prepare by other synthetic routes.

The formation of ordered nanostructures critically depends on the interfacial interactions between the surfactants and the inorganic species. The initial Mobil (MCM-41 series) silicate-based materials were prepared using direct ionic bonding with a cationic surfactant [1,2]. Apparently, nanoporous silicates can be synthesized under a variety of experimental conditions. A more generalized synthesis route was developed to include ion-mediated ionic bonding, in which the surfactants and the ceramics are similarly charged and bind together through an intermediate ionic species of opposite charge [13,14]. Neutral surfactants can also be used [15,16]. The neutral synthesis route used uncharged (dodecyl amine) or nonionic surfactants (polyethylene oxide). The oxide precursor was bonded to the surfactant through hydrogen bonding. This produced nanoporous materials with thick walls and small grain sizes. Other approaches, including amphoteric surfactant [17] and ligand-assisted templating using amine surfactant, were also developed to prepare transition-metal mesoporous materials (niobium and tantalum oxides) [18, 19]. In the ligand-assisted templating approach the ceramics (alkoxide) was covalently bonded to the long-chain amine surfactant before the hydrolysis and condensation of the precursor. This approach allows the selective hydrolysis and condensation of the oxide precursor on the micellar surface and prevents the uncontrolled precipitation of particulate oxide materials that is commonly observed in nonsilicate materials.

INTERFACIAL CHEMISTRY IN ORDERED NANOCOMPOSITES

The ordered nanoporous materials provide an ideal platform to form more complicated nanocomposites. There has been a growing interest in nanocomposites because of the unique electronic, magnetic, optical, and chemical properties related to the size and the microstructural arrangement of such materials [20, 21]. For example, nanoscale magnetic materials have been explored for applications in information storage, color imaging, ferrofluids, and magnetic refrigeration [22–24]. Although many methods have been developed to synthesize nanocomposites using colloidal processing [25, 26], gas phase condensation, precipitation within nanoporous polymers or ceramics [27], and infiltration of microporous zeolite materials [28], a major problem is the precise control of size, shape, and spatial arrangement of nanoparticles. The recent discovery of the ordered nanoporous silicate materials provides a unique opportunity to design and engineer nanophase composites.

We have synthesized ordered magnetic nanocomposites ($NiO–SiO_2$) based on nanoporous silica using the impregnation-to-incipient-wetness technique. A high magnetic permeability was obtained due to the alignment of the rod-like particles within the hexagonal porous matrix. Furthermore, the interfacial atomic structure is characterized by transmission electron microscopy (TEM) and energy loss fine structure (ELFS) analysis. Similar methods can be used to produce other metal–ceramic and ceramic–ceramic composite materials.

The mesoporous silica was synthesized according to standard methods, using cetyltrimethylammonium chloride ($C_{16}H_{33}(CH_3)_3NOH/Cl$), colloidal silica (HiSil–233), and tetramethylammonium silicate. This mixture was reacted at 105 °C in a sealed Teflon container for 3 to 5 days and calcined at 540 °C for 7 hr in air. X-ray diffractometry (XRD) suggests that the material has hexagonal ordering with a periodicity of 4 nm. N_2 adsorption/desorption isotherms indicate a surface

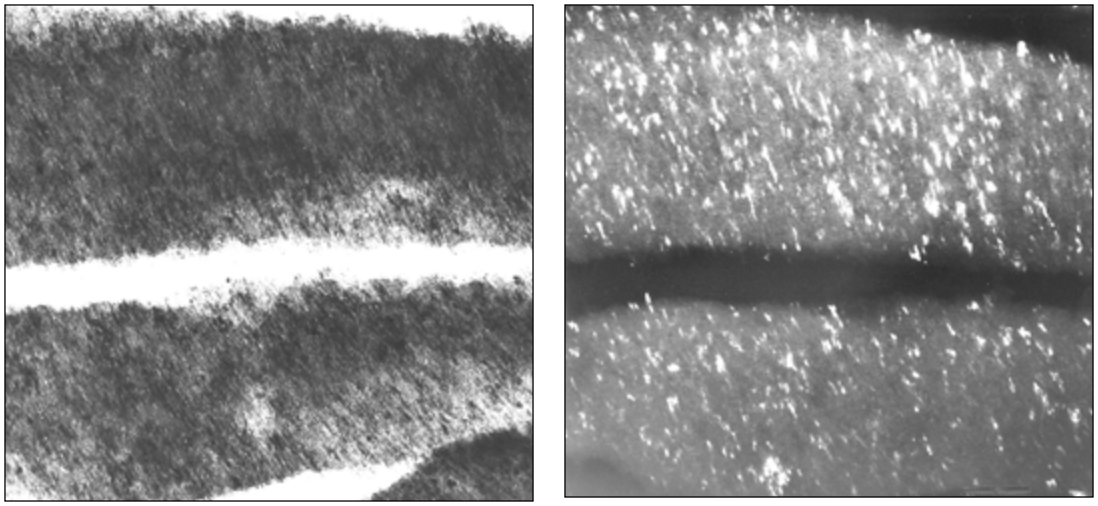

(a) (b)

Fig. 1 TEM images of $NiO–SiO_2$ composite: (a) is the bright field image and (b) is the dark field image. The particles are uniformly distributed, and have a rod-like shape. The size of the crystals in the dark field image is about 2 nm.

area of 900 m^2/g and a pore size of 2.8 nm. The $NiO–SiO_2$ composite (7% Ni by weight) was prepared using the impregnation-to-incipient-wetness techniques [29]. NiO was chosen as a model system for its simple crystalline structure (cubic, a = 4.18 Å). Other materials, such as Fe_2O_3, may have several crystalline structural forms, thus complicating the interpretation of the results. A solution of nickel nitrate ($Ni(NO_3)_2.6H_20$), was prepared. The volume of the nitrate solution approximately corresponded to the total pore volume of the mesoporous SiO_2 support. The nanoporous SiO_2 powders were tumbled, and the solution of nickel nitrate was added dropwise. Capillary forces ensured that the liquid permeated the entire porous structure. This technique allowed accurate control of the amount of the metal that was incorporated into the porous support. The resulting composite was dried at 100 °C overnight in a vacuum oven and then calcined at 350 °C for 1 hr.

The samples were embedded in a fixing epoxy resin and sectioned with a diamond knife on an ultramicrotome. TEM work was performed on a JEOL 2010 FEG microscope at 200 KeV. The electron energy loss spectra (EELS) were obtained on a Philips 430 TEM equipped with a Gatan PEELS model 666 system at 200 KeV in the diffraction mode. Gatan EL/P 2.1 software with a custom function AcqLong [30] was used for data acquisition to reduce statistical and systematical noise. UW EXAFS 3.0 software [31] was used for data analysis. The magnetic hysteresis loops were measured on a Lakeshore Model 73 Vibrating Sample Magnetometer (VSM). When the NiO precursor infiltrated the silica matrix, it assumed the hexagonal arrangement and the geometry of the pores. The micrographs in Fig. 1 are the edge-on TEM images of the $NiO–SiO_2$ composite. The horizontal crack was caused by microtoming. The nanoparticles are uniformly distributed and the parallel pore channels are darkened by the infiltrated phase. The bright field image (Fig. 1a) and the dark field image (Fig. 1b) clearly illustrate that the particles are aligned along the pore channels and have a rod-like shape. The dark field suggests that the crystals have a diameter about 2 nm, and a length up to 30 nm. In some areas large particles are observed because individual crystals cannot be resolved when they overlap. Selected electron diffraction pattern (SAD) confirms that the crystalline phase is NiO (cubic, a = 4.18 Å).

(a)

(b)

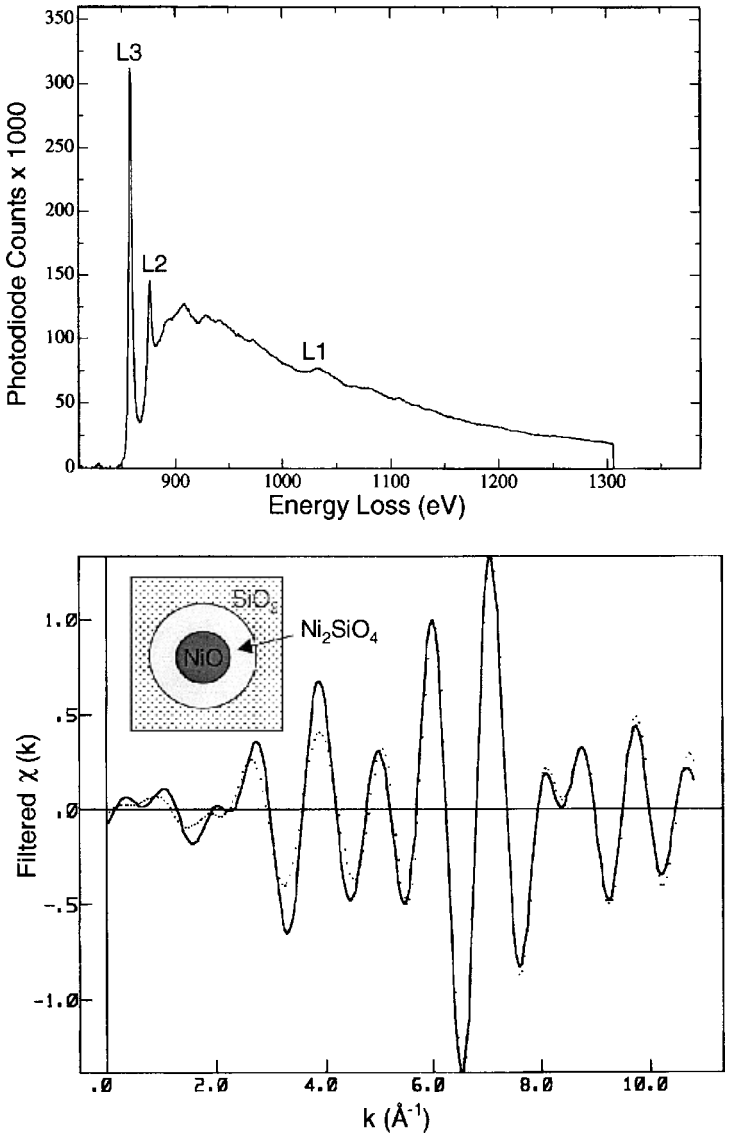

Fig. 2 EELS and ELFS results of the NiO–SiO_2 composites: (a) is the Ni L-edge spectrum with the pre-edge background removed and (b) is the filtered fine structure χ(k). The solid line is the experimental data, and the dotted line is the fitted result. The r-space nonlinear least-squares fit was performed in an r-range from 1.7 to 3.8 Å and a k-range from 3 to 10.4 $Å^{-1}$ with 12 independent points and 9 parameters. The best fit was produced by a molar composition of 75% NiO and 25% Ni_2SiO_4.

Figure 2a is a typical electron energy loss (EEL) spectrum for the Ni L-edge. This spectrum was first treated to remove the post-edge background and normalized, and then Fourier transformed to r-space. The r-space nonlinear least-squares fit was performed using the FEFF6 model (a computer program that calculates the theoretical energy loss fine structures (ELFS) and X-ray absorption fine structures (XAFS)) [32]. Additional peaks were observed in the radial distribution function of the composite as compared to that of a standard NiO, suggesting a mixed phase. Therefore, a three-component

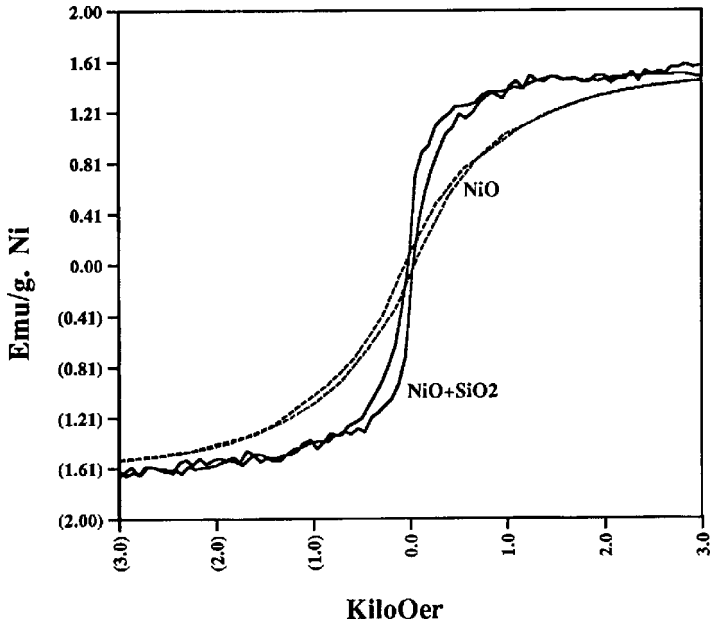

Fig. 3 Magnetization curves of the standard NiO and the NiO–SiO_2 composite. As compared to the standard NiO, the composite material shows a rapid change in the magnetization when the field is changed and saturates at a low magnetic field. This result suggests that the composite material has a higher magnetic permeability due to the alignment of the particles.

model consisting of Ni, NiO and Ni_2SiO_4 (orthorhombic, a = 5.91 Å, b = 10.12 Å, c = 4.73 Å) [33] was then used to fit the unknown data. The final results were plotted in the filtered $\chi(k)$ in Fig. 2b. The best fit is produced by a molar composition of 75% of NiO plus 25% Ni_2SiO_4 with an insignificant amount of Ni. The dotted line is the result from the fit, and the solid line is the experimental result. The fit also suggests that all atomic distances of Ni–O, Ni–Ni and Ni–Si are expanded by about 3%, which agrees with the results by a previous ELFS study of the atomic structure of fine metallic particles [34]. Based on this composition it can be calculated that the dispersed particles consist of a core of crystalline NiO with a diameter of 1.9 nm and an outer interfacial layer of Ni_2SiO_4 about 0.45 nm in thickness, as shown in the insert in Fig. 2b. The Ni_2SiO_4 interface layer is amorphous. This is consistent with the TEM results in Fig. 1. The bright field shows both the crystalline NiO core and the amorphous Ni_2SiO_4 layer. The dark field image only shows the crystalline phase.

The magnetic hysteresis loops of the NiO–SiO_2 and the standard NiO material were measured, and the results were plotted in Fig. 3. The standard NiO material is made of particles ranging from submicrometer to several micrometers in size. The magnetization gradually increases with the magnetic field and does not saturate until 3 KiloOer. In contrast, for the NiO–SiO_2 composite the magnetization changes rapidly when the magnetic field is increased or decreased, and the magnetization saturates at less than ±1 KiloOer. This behavior shows that the NiO–SiO_2 nanocomposite has a higher magnetic permeability than the standard NiO powders. The rapid magnetization behavior is also different from nanoscale magnetic materials prepared by other methods. Such materials show gradual magnetization in a field because of the wide particle size distribution and random orientation. On the contrary, in the new nanocomposite material the magnetic particles are uniformly distributed and aligned in the same direction along the pore channels within the mesoporous silica particles. These mesoporous silica particles are several micrometers in size and can rotate in a magnetic field. This will result in a higher

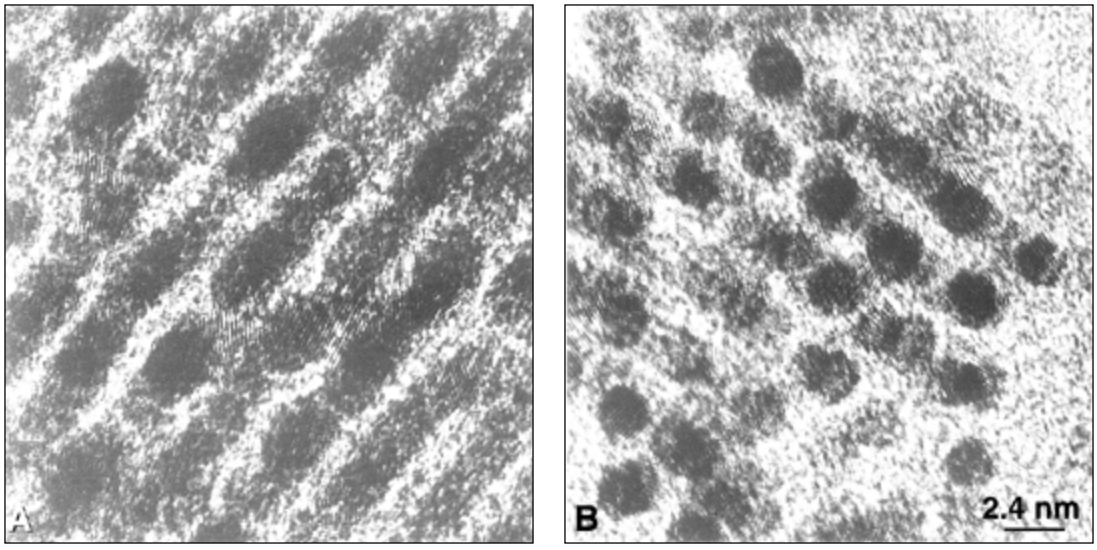

Fig. 4 High-resolution TEM image of a Pd–SiO_2 composite: (a) is the cross-section along the longitudinal direction of the Pd particles and (b) is the cross-section perpendicular to the long axis. Both images show the lattice fringes of the Pd particles, which have a uniform size, and are well ordered (from ref. 4 with permission).

magnetic permeability. Therefore, the nanocomposite has the ideal microstructure for a magnetic material: rod-like shape separated by the matrix, uniform size, and particle alignment [35].

We believe that ordered mesoporous materials will form the basis of a new generation of ordered ceramic–ceramic and metal–ceramic nanocomposites. These materials will have unique optical, electronic, and magnetic properties. For example, Fig. 4 shows the ordered microstructure of a Pd–SiO_2 composite. Figure 4a is the cross-section image parallel to the pore channels, and Fig. 4b is the cross-section image perpendicular to the pore channels. Both images show the lattice fringes of the ordered nanoparticles.

INTERFACIAL CHEMISTRY IN SELF-ASSEMBLED MOLECULAR MONOLAYERS IN ORDERED NANOPOROUS MATERIALS

Many applications have been considered for the new nanoporous materials, including energy storage, catalysis, adsorption, ion exchange, sensing controlled release, etc. However, most of the applications require the materials to have specific binding sites, stereochemical configuration or charge density, and acidity [36–38]. Most nanoporous materials do not themselves have the appropriate surface properties.

A new class of hybrid nanoscale materials has been developed based on the assembly of organized molecular monolayers in ordered nanoscale materials [39–42]. This approach allows us to systematically modify the surface chemistry and tailor the molecular recognition process of mesoporous materials toward the targets. In this approach, high-quality, oriented molecular monolayers are spontaneously grown on ordered nanoporous ceramic substrates with controlled pore shape and pore size. The functional molecules are closely packed and cross-linked with one another. The terminal functional groups on the monolayer can be easily modified, thereby allowing rational design and layer-by-layer construction of host sites on the nanoporous substrates that match the shape, size, or chemical properties of heavy metals, transition metals, or organic molecules, and as such, making them extremely efficient scavengers of these species, or effective catalysts for reactions involving these species.

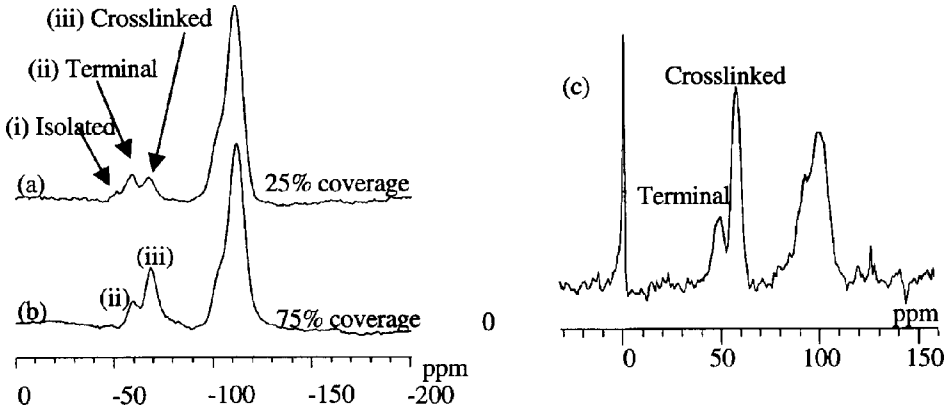

Fig. 5 ^{29}Si NMR spectra of functionalized mesoporous silica. (a) 50 Å nanoporous silica with low degree of hydration and low monolayer coverage (25%). (b) 50 Å nanoporous with a higher degree of hydration and a higher coverage. (c) 50 Å nanoporous silica using supercritical CO_2 as the reaction medium. A high degree of cross-linking density suggests better packing of the monolayer molecules (a and b are from ref. 39 with permission from *Science*.)

The quality of the molecular monolayer is reflected on the interfacial binding between the monolayer and the silica substrate. High-quality, close-packed monolayers can be formed on the nanoporous supports through the introduction of several layers of physically adsorbed waters on the nanoporous surface. The role of the water molecules is to physically confine all the hydrolysis and condensation reactions of the organosilianes at the interface. Currently, we can systematically vary the population densities of functional groups on the nanoporous materials from 10% up to 100% of the full surface coverage. Figures 5a and 5b compare the ^{29}Si NMR spectra obtained from the nanoporous silica functionalized with tris(methoxy)mercaptopropylsilane (TMMPS). Based on NMR and other studies, we can conclude that with a low degree of hydration, the functional molecules only cover part of the surface (25% coverage). The siloxane groups can adopt three different conformations: (i) isolated groups that are not bound to any neighboring siloxanes, (ii) terminal groups that are only bound to one neighboring siloxane, and (iii) cross-linked groups that are bound to two neighboring siloxanes. Among these three groups, the terminal conformation is dominant. With a higher degree of hydration, a high surface-population density can be achieved. NMR spectra for ^{29}Si show the predominance of only cross-linked bonding conformation for the siloxanes, rather than a distribution of isolated, terminal, and cross-linked groups. The supercritical fluid (SCF) process further improved the quality and the chemical stability of the monolayers on mesoporous silica. SCF fluids offer a unique environment to perform chemical reaction because of the liquid-like solvation properties and gas-like physical properties (viscosity, diffusivity) [43]. The low density, low viscosity, high diffusivity, and low surface tension of SCF fluids make them ideal media for performing silanation of the internal surfaces of porous materials. CO_2 is environmentally benign, nontoxic, nonflammable, and inexpensive. The mild critical conditions for CO_2 (Tc = 31.1 °C, Pc = 73.8 bar) can be easily attained, and are unlikely to cause degradation of the porous substrates. Due to direct pressure pumping, the silanes are readily delivered to the internal pore surface. Similarly, when the pressure is decreased, the unreacted silanes and by-products are forced out of the inner volume of the porous substrate. Figure 5c is the ^{29}Si NMR spectrum of the supercritically functionalized mesoporous silica. Compared to Fig. 5b, the peak corresponding to the cross-linked siloxanes is much more pronounced, indicating a high degree of cross-linking.

The interfacial chemistry can be easily tuned for different applications. For example, Fig. 6 shows two different types of functional molecules on the silica substrate. Figures 6a and 6b involve a direct chemical bonding between heavy metals and alkyl thiols [tris(methoxy)mercaptopropylsilane, TMMPS]

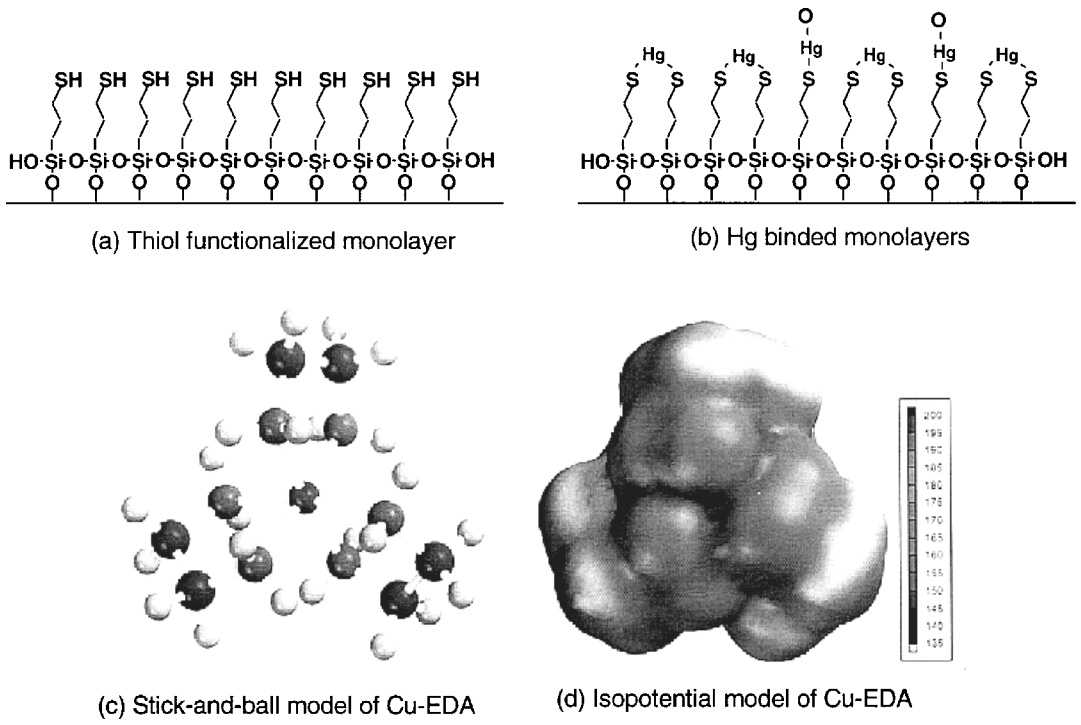

Fig. 6 Two different types of functional monolayers in ordered nanoporous silica: (a) Thio-functionalized monolayers. (b) Heavy metal binding on the monolayer. The metal ions directly bind to the thiol groups on the monolayer, forming an efficient heavy metal trap. (c) Stick-and-ball model of Cu–EDA complex on silica substrate. (d) Isopotential surface for Cu–EDA complex. The Cu(II)–EDA complex forms an ideal three-fold symmetry cage structure for binding tetrahedral anions (from Ref. 39 and Ref. 46 with permission).

as the functional molecules for heavy-metal adsorption. Mercury and heavy-metal contamination is a serious problem at waste-contaminated sites of the U.S. Department of Energy [44]. Industrial and civilian sources deposit a large amount of mercury into the environment every year [45]. The thiol–silica hybrid nanoporous materials thus produced can efficiently remove mercury and other heavy metals (such as lead and silver) from contaminated aqueous and organic solutions. The distribution coefficient, Kd, has been measured as high as 10^8. (Kd is defined as the amount of adsorbed metal (μg) on 1 g of adsorbing material, divided by metal concentration (μg/ml) remaining in the treated waste stream). The exceptional selectivity and capability of hybrid materials to remove mercury and other heavy metals from contaminated solutions have been demonstrated under a wide range of conditions (water, oil, acidic, neutral, and basic solvents). A loading capacity of 600 mg (Hg)/g (absorbing materials) has been obtained. A single treatment of highly contaminated water usually reduced the mercury concentration to well below U.S. Environmental Protection Agency (EPA) elemental limits for hazardous wastes and even drinking-water standards. Similar results have also been obtained for lead and silver, which are major concerns in drinking water. The performance of the materials is not affected by the presence of background electrolytes (ions of barium, zinc, sodium, or nitrate).

Another application is arsenate removal [46]. Recent reports of the crisis caused by arsenic contamination of drinking water in Bangladesh and other parts of the world have attracted wide public attention [47,48]. In Bangladesh alone, and estimated 50 to 70 million people could be affected by drinking water contaminated by natural arsenic sources. Arsenic, along with other toxic metals like

chromium, and selenium, are included in the EPA's list of priority pollutants. These contaminating species, unlike many heavy metals and transition metals, can exist in nature as tetrahedral oxyanions (arsenate ions $HAsO_4^{2-}$, $H_2AsO_4^{1-}$, and chromate ions $HCrO_4^-$, CrO_4^{2-}) [49]. In many cases, trace amounts of arsenate and chromate need to be removed from waste solutions containing high concentrations of competing anions, sulfate, and chloride in particular. Currently, the development of effective anion binding materials is an important subject in chemistry, biochemistry, materials and environmental science [50,51]. We synthesized and used metal-chelated ligands immobilized on mesoporous silica as an efficient anion binding material for both arsenate and chromate. The mesoporous silica was functionalized with an ethylenediamine (EDA) terminated silane [(2 aminoethyl,)-3-aminopropyl trimethyl silane]. Cu(II) ions were binded to the EDA monolayer with a 3 to 1 EDA to Cu ratio, forming an approximately octahedral $Cu(EDA)_3$ complex structure. The cationic octahedral complex contains an electrophilic basket with C3 symmetry that forms an ideal host for a tetrahedral anion. Nearly complete removal of arsenate and chromate has been achieved in the presence of competing anions for solutions containing up to 100 ppm toxic metal anions under a variety of experimental conditions. Good selectivity between chromate (or arsenate) and sulfate ions can be achieved at high anion concentrations. Anion loading is more than 120 mg (anion)/g of adsorption materials. The anion loading capacity of this material is comparable (on a molar basis) to the heavy metal loading capacity achieved with the best cation sorbent materials (functionalized mesoporous silica) discussed earlier, when the stoichiometry of binding and the atomic/molecular weight of the target species are taken into consideration. This approach is especially promising considering the rich chemistry that can be explored with monolayers [52,53], with mesoporous silica, and the possibility of designing better anion-recognition ligands.

SUMMARY

Interfacial reactions and interfacial chemistry play a critical role in the formation, the self-assembly, and the properties of ordered nanoscale materials. The examples given in this paper illustrate how the specific interactions between surfactants and inorganic–organic species affect the formation of different phases that can be derived. Furthermore, this paper also briefly discussed the formation of functional molecular monolayers in ordered nanoscale materials, and the critical role the interface plays on the organization, the quality, and the properties of the monolayers. In nanoscale materials, a large number of atoms reside in the interfacial region and may assume a different chemical environment from the atoms outside the interfacial region. The fine interfacial atomic structures are illustrated in the formation of ordered nanomagnet nanocomposites. In all the examples shown in this paper, the ordered nanoscale materials offer distinct advantages over traditional nanocomposites. The ability to further tailor the interfacial interactions and interfacial properties will lead to more sophisticated functional nanoscale materials.

ACKNOWLEDGMENT

This work is supported by the Office of Basic Energy Sciences, Division of the Materials Sciences, of the U.S. Department of Energy. Pacific Northwest National Laboratory is operated by Battelle Memorial Institute for the U.S. Department of Energy under Contract DE-AC06-76RL01830.

REFERENCES

1. J. S. Beck, J. C. Vartuli, R. J. Roth, M. E. Leonowicz, C. T. Kresge, T-W Chu, D. H. Olson. *J. Am. Chem. Soc*. **114**, 10834 (1992).
2. C. T. Kresge, M. E. Leonowicz, W. J. Roth, J. C. Vartuli, J. S. Beck. *Nature* **359**, 710 (1992).

3. J. S. Beck and J. C. Vartuli. *Curr. Opin. Sol. St. Mater. Sci.* **1**, 76 (1996).
4. J. Liu, A. Y. Kim, L. Q. Wang, B. J. Palmer, Y. L. Chen, P. Bruinsma, B. C. Bunker, G. J. Exarhos, G. L. Graff, P. C. Rieke, G. E. Fryxell, J. W. Virden, B. J. Tarasevich, L. A. Chick. *Adv. Colloid. Interface Sci.* **69**, 131 (1996).
5. N. K. Raman, M. T. Anderson, C. J. Brinker. *Chem. Mater*. **8**, 1682 (1996).
6. J. Israelachvili. *Intermolecular & Surface Forces*, 2nd edition, Chapters 16, 17, and 18, Academic Press, San Diego (1991).
7. D. F. Evans and H. Wennerstrom. *The Colloidal Domain, Where Physics, Chemistry, Biology, and Technology Meet*, Chapter 2, VCH, New York (1994).
8. P. K.Vinson, J. R. Bellare, H. T. Davis, W. G. Miller, L. E. Scriven. *J. Colloid Interface Sci*. **142**, 74 (1991).
9. Q. Huo, D. I. Margolese, U. Ciesla, P. Feng, T. E. Gier, P. Sieger, R. Leon, P. M. Petroff, F. Schuth, G. D. Stucky. *Nature* **368**, 317 (1994).
10. P. Yang, D. Zhao, D. I. Margolese, B. F. Chmelka, G. D. Stucky. *Nature* **396**, 152 (1998).
11. R. E. Newnham. *Adv. Ceram. Mater*. **3**, 12 (1998).
12. D. H. Gray, S. Hu, E. Juang, D. L. Gin. *Adv. Mater.* **9**, 731 (1997).
13. Q. Huo, D. I. Margolese, U. Ciesla, P. Feng, T. E. Gier, P. Sieger, R. Leon, P. M. Petroff, F. Schuth, G. D. Stucky. *Nature* **368**, 317 (1994).
14. Q. Huo, R. Leon, P. M. Petroff, G. Stucky. *Science* **268**, 1324 (1995).
15. P. T. Tanev and T. J. Pinnavaia. *Science* **267**, 865 (1995).
16. S. A. Bagshaw, E. Prouzet, T. J. Pinnavia. *Science* **267**, 865 (1995).
17. A. Y. Kim, P. Bruinsma, Y. Chen, L.-Q. Wang, J. Liu. *Chem. Commun*. 161, (1997).
18. D. M. Antonelli and J. Y. Ying. *Chem. Mater*. **8**, 874 (1996).
19. D. M. Antonelli and J. Y. Ying, *Angew. Chem. Int. Ed. Engl*. **34**, 2014 (1995).
20. R. E. Newnham. *Ferroelectrics*, **68**, 1 (1986).
21. K. Uchino, E. Sadanaga, T. J. Hirose, *J. Am. Ceram. Soc*. **72**, 1555 (1989).
22. R. F. Ziolo, E. P. Giannelis, B. E. Weinstein, M. P. O'Horo, B. N. Ganuly, V. Mehrotra, M. W. Russel, D. R. Husffman. *Science* **258**, 414 (1992).
23. D. D. Awschalom, D. P. Divincenzo, J. F. Smyth. *Science* **258**, 414 (1992).
24. J. K. Vassiliou, V. Mehrotra, M. W. Russell, R. D. McMichael R. D. Shull, R. F. Ziolo. *J. Appl. Phys*, **73**, 5109 (1993).
25. J. Liu, W. Y Shih, M. Sarikaya, I. A. Aksay. *Phy. Rev. A*. **41**, 3206 (1990).
26. J. Liu, M. Sarikaya, W. Y Shih, I. A. Aksay. *Mater. Res. Soc. Symp. Proc*. **175**, 3 (1992).
27. For example: R. D Shull, J. J., Ritter, A. J. Shapio, L. J. Swartzendruber, L. H. Bennett. *Mat. Res. Soc. Sym. Proc*. **206**, 455 (1991).
28. For a review, see G. A. Ozin. *Adv. Mater.* **4**, 612 (1992).
29. C. N. Satterfield. *Heterogeneous Catalysis in Industrial Practice*, 2nd Edition, 107, McGraw-Hill, New York (1991).
30. M. Qian, M. Sarikaya, E. A. Stern. *Proceedings of the 51th Annual Meeting of the Microscopy Society of America*, 578, San Francisco Press, San Francisco (1993); M. Qian, M. Sarikaya, E. A. Stern. *Ultramicroscopy* **59**, 137 (1995).
31. Information regarding this software may be obtained from Professor E. A. Stern, Department of Physics, University of Washington, Seattle, WA.
32. J. J. Rehr, R. C. Albers, S. I. Zabinsky. *Phys. Rev. Lett*. **69**, 3397 (1992).

33. R. W. Wyckoff. *Crystal Structures*, Interscience Publication, New York (1963).
34. M. Diociaiuti, P. Picozzi, S. Santucci, L. Lozzzi, M. D. Crescenzi. *J. Microscopy*, **166**, 231–245 (1991).
35. O. T. Paine. *Magnetic Properties of Metals and Alloys*, Chapter 8, American Society for Metals, Cleveland, Ohio (1959).
36. A. Sayari. *Chem. Mater*. **8**, 1840 (1996).
37. R. G. Anthony, C. V. Philips, R. G. Dosch. *Waste Management* **13**, 503 (1993).
38. K. D. Schierbaum , T. Weiss, E. U. Thoden van Velzen, J. F. J. Engbersen, D. N. Reinhoudt, W. Gopel. *Science* **265**, 1413 (1994).
39. X. Feng, G. E. Fryxell, L. Q. Wang, A. Y. Kim, K. Kemner, J. Liu. *Science* **276**, 923 (1997).
40. J. Liu, X. Feng, G. E. Fryxell, L. Q. Wang, A. Y. Kim, M. Gong. *Adv. Mater.* **10**, 161 (1998).
41. L. Mercier and T. Pinnavaia. *Adv. Mater.* **9**, 500(1997).
42. L. Mercier and T. Pinnavaia. *J. Envir. Sci. Technol*. **32**, 2749 (1998).
43. See articles in "Supercritical Fluids," R. Noyori, ed., *Chem. Rev.* **99**, (1999).
44. J. E. Klein. R&D Needs for Mixed Waste Tritium Pump Oils (U), Westinghouse Savannah River Company Inter-Office Memorandum, SRT-HTS-94-0235, July 11 (1994).
45. S. Mitra. *Mercury in the Ecosystem*, Trans Tech Publications, Lancaster, PA (1986).
46. G. E. Fryxell, J. Liu, T. A. Hauser, Z. Nie, K. F. Feris, S. Mattigod. *Chem. Mater*. **11**, 2148 (1999).
47. R. Nickson, J. McArthur, W. Burgess, K. M. Ahmed, P. Ravenscroft, M. Rahman. *Nature* **395**, 338 (1998).
48. http://bicn.com/acic, 1999.
49. C. F. Baes, Jr. and R. E. Mesmer. *The Hydrolysis of Cations*, pp. 215, 366–368, John Wiley, New York (1976).
50. E. A. Woolson. *Biological and Environmental Effects of Arsenic*, B. A. Fowler, ed., pp. 51–120, Elsevier, New York (1983).
51. J. L. Atwood, K. T. Holman, J. W. Steed. *Chem. Commun*. 1401 (1996).
52. G. M. Whitesides. *Sci. Am*. **273**, 146 (1995).
53. A. Ulman. *Chem. Rev*. **96**, 1533 (1996).